Draft: September 23, 2014
Preprint typeset using LaTeX style emulateapj v. 5/2/11

arXiv:1405.5524v2 [astro-ph.CO] 21 Sep 2014

THE ATACAMA COSMOLOGY TELESCOPE: CMB POLARIZATION AT $200 < \ell < 9000$

Sigurd Naess[1], Matthew Hasselfield[2,3], Jeff McMahon[4], Michael D. Niemack[5], Graeme E. Addison[3], Peter A. R. Ade[6], Rupert Allison[1], Mandana Amiri[3], Nick Battaglia[7], James A. Beall[8], Francesco de Bernardis[5], J Richard Bond[9], Joe Britton[8], Erminia Calabrese[1], Hsiao-mei Cho[8], Kevin Coughlin[4], Devin Crichton[10], Sudeep Das[11], Rahul Datta[4], Mark J. Devlin[12], Simon R. Dicker[12], Joanna Dunkley[1], Rolando Dünner[13], Joseph W. Fowler[8], Anna E. Fox[8], Patricio Gallardo[5,13], Emily Grace[14], Megan Gralla[10], Amir Hajian[9], Mark Halpern[3], Shawn Henderson[5], J. Colin Hill[2], Gene C. Hilton[8], Matt Hilton[15], Adam D. Hincks[3], Renée Hlozek[2], Patty Ho[14], Johannes Hubmayr[8], Kevin M. Huffenberger[16], John P. Hughes[17], Leopoldo Infante[13], Kent Irwin[18], Rebecca Jackson[4,19], Simon Muya Kasanda[15,20], Jeff Klein[12], Brian Koopman[5], Arthur Kosowsky[21], Dale Li[8], Thibaut Louis[1], Marius Lungu[12], Mathew Madhavacheril[22], Tobias A. Marriage[10], Loïc Maurin[13], Felipe Menanteau[23,24], Kavilan Moodley[15], Charles Munson[4], Laura Newburgh[14], John Nibarger[8], Michael R. Nolta[9], Lyman A. Page[14], Christine Pappas[14], Bruce Partridge[25], Felipe Rojas[13,26], Benjamin L. Schmitt[12], Neelima Sehgal[22], Blake D. Sherwin[27], Jon Sievers[20,9], Sara Simon[14], David N. Spergel[2], Suzanne T. Staggs[14], Eric R. Switzer[28,9], Robert Thornton[29,12], Hy Trac[7], Carole Tucker[6], Masao Uehara[26], Alexander Van Engelen[22], Jonathan T. Ward[12], Edward J. Wollack[28]

Draft: September 23, 2014

ABSTRACT

We report on measurements of the cosmic microwave background (CMB) and celestial polarization at 146 GHz made with the Atacama Cosmology Telescope Polarimeter (ACTPol) in its first three months of observing. Four regions of sky covering a total of 270 square degrees were mapped with an angular resolution of $1.3'$. The map noise levels in the four regions are between 11 and 17 μK-arcmin. We present TT, TE, EE, TB, EB, and BB power spectra from three of these regions. The observed E-mode polarization power spectrum, displaying six acoustic peaks in the range $200 < \ell < 3000$, is an excellent fit to the prediction of the best-fit cosmological models from WMAP9+ACT and *Planck* data. The polarization power spectrum, which mainly reflects primordial plasma velocity perturbations, provides an independent determination of cosmological parameters consistent with those based on the temperature power spectrum, which results mostly from primordial density perturbations. We find that without masking any point sources in the EE data at $\ell < 9000$, the Poisson tail of the EE power spectrum due to polarized point sources has an amplitude less than 2.4 $\mu\mathrm{K}^2$ at $\ell = 3000$ at 95% confidence. Finally, we report that the Crab Nebula, an important polarization calibration source at microwave frequencies, has 8.7% polarization with an angle of $150.7^\circ \pm 0.6^\circ$ when smoothed with a $5'$ Gaussian beam.

[1] Sub-Department of Astrophysics, University of Oxford, Keble Road, Oxford, UK OX1 3RH
[2] Department of Astrophysical Sciences, Peyton Hall, Princeton University, Princeton, NJ USA 08544
[3] Department of Physics and Astronomy, University of British Columbia, Vancouver, BC, Canada V6T 1Z4
[4] Department of Physics, University of Michigan, Ann Arbor, USA 48103
[5] Department of Physics, Cornell University, Ithaca, NY, USA 14853
[6] School of Physics and Astronomy, Cardiff University, The Parade, Cardiff, Wales, UK CF24 3AA
[7] McWilliams Center for Cosmology, Carnegie Mellon University, Department of Physics, 5000 Forbes Ave., Pittsburgh PA, USA, 15213
[8] NIST Quantum Devices Group, 325 Broadway Mailcode 817.03, Boulder, CO, USA 80305
[9] Canadian Institute for Theoretical Astrophysics, University of Toronto, Toronto, ON, Canada M5S 3H8
[10] Dept. of Physics and Astronomy, The Johns Hopkins University, 3400 N. Charles St., Baltimore, MD, USA 21218-2686
[11] Department of High Energy Physics, Argonne National Laboratory, 9700 S Cass Ave, Lemont, IL USA 60439
[12] Department of Physics and Astronomy, University of Pennsylvania, 209 South 33rd Street, Philadelphia, PA, USA 19104
[13] Departamento de Astronomía y Astrofísica, Pontificía Universidad Católica, Casilla 306, Santiago 22, Chile
[14] Joseph Henry Laboratories of Physics, Jadwin Hall, Princeton University, Princeton, NJ, USA 08544
[15] Astrophysics and Cosmology Research Unit, School of Mathematics, Statistics and Computer Science, University of KwaZulu-Natal, Durban 4041, South Africa
[16] Department of Physics, Florida State University, Tallahassee FL, USA 32306
[17] Department of Physics and Astronomy, Rutgers, The State University of New Jersey, Piscataway, NJ USA 08854-8019
[18] Department of Physics, Stanford University, Stanford, CA, USA 94305-4085
[19] School of Earth and Space Exploration, Arizona State University, Tempe, AZ, USA 85287
[20] Astrophysics and Cosmology Research Unit, School of Chemistry and Physics, University of KwaZulu-Natal, Durban 4041, South Africa
[21] Department of Physics and Astronomy, University of Pittsburgh, Pittsburgh, PA, USA 15260
[22] Physics and Astronomy Department, Stony Brook University, Stony Brook, NY USA 11794
[23] National Center for Supercomputing Applications (NCSA), University of Illinois at Urbana-Champaign, 1205 W. Clark St., Urbana, IL, USA, 61801
[24] Department of Astronomy, University of Illinois at Urbana-Champaign, W. Green Street, Urbana, IL, USA, 61801
[25] Department of Physics and Astronomy, Haverford College, Haverford, PA, USA 19041
[26] Sociedad Radiosky Asesorías de Ingeniería Limitada Lincoyán 54, Depto 805 Concepción, Chile
[27] Berkeley Center for Cosmological Physics, LBL and Department of Physics, University of California, Berkeley, CA, USA 94720
[28] NASA/Goddard Space Flight Center, Greenbelt, MD, USA

1. INTRODUCTION

The standard ΛCDM model of cosmology is now well established (e.g., Spergel et al. 2003; Planck Collaboration 2013c). The model is geometrically flat and dark-energy dominated, with baryons comprising about 15% of the total matter density. The initial fluctuations are adiabatic, Gaussian, and nearly scale-free. The free parameters of the model have been determined to high precision, largely from measurements of the cosmic microwave background (CMB) temperature anisotropies on angular scales from the full sky down to a few arcminutes (Hinshaw et al. 2013; Planck Collaboration 2013c; Sievers et al. 2013; Hou et al. 2014). Large-scale structure measurements of the baryon acoustic oscillation scale (e.g., Anderson et al. 2014) and direct measurements of the expansion rate and acceleration from type-Ia supernova observations (e.g., Suzuki et al. 2012; Betoule et al. 2014) also provide constraints. While the model is in generally good agreement with all cosmological probes, there are some mild tensions at the 2σ to 3σ level (e.g., Planck Collaboration 2013c) and possible hints of "anomalies" (e.g., Planck Collaboration 2013d; Bennett et al. 2011; Copi et al. 2010). Further precise tests of the model are clearly needed.

The polarization of the CMB provides a complementary source of information and also probes cosmological physics beyond what can be obtained with temperature alone. The E-mode polarization power spectrum (Kamionkowski et al. 1997; Zaldarriaga & Seljak 1997) arises primarily from the motions of the primordial plasma at the epoch of last scattering (redshift $z = 1100$), with a contribution at large angular scales from perturbations at the reionization epoch ($z \approx 10$). Precision measurements of the acoustic features in the E-mode polarization power spectrum provide a non-trivial confirmation of the acoustic oscillations in the early universe seen in temperature data. Rocha et al. (2004) and Galli et al. (2014) point out that with the CMB E-mode polarization alone one may place stronger constraints on cosmological parameters than with the temperature anisotropy. More importantly, the combination of temperature and polarization data constrain a range of physical effects beyond the standard model. For example, primordial isocurvature perturbations alter the phase of the oscillations in polarization relative to temperature compared to pure adiabatic perturbations (e.g., Bond & Efstathiou 1987; Bucher et al. 2004; MacTavish et al. 2006; Sievers et al. 2007). The additional sensitivity to the standard cosmological model provides increased ability to probe neutrino properties, early dark energy, and time variation of fundamental constants. Comparison of temperature and polarization data also probes cosmological effects which affect the two in different ways, such as the kinematic Sunyaev-Zeldovich effect (Calabrese et al. 2014).

Polarization observations can also characterize the B-mode fluctuations, which are not generated by the dominant primordial density perturbations. B-mode polarization contains a signal from gravitational lensing by all structure along the line of sight, for multipoles $\ell > 200$ (Zaldarriaga & Seljak 1998). The B-mode fluctuations also reflect other new physical effects, such as cosmic birefringence due to magnetic fields (Kosowsky et al. 2005) or photon couplings beyond the standard model (Lue et al. 1999). A definitive detection of primordial B-mode polarization at $\ell < 200$ from tensor perturbations generated by inflation will test the fundamental nature of the gravitational force and probe energy scales well beyond terrestrial experiments.

Although *WMAP* has made the only published measurement of large-angle E-mode polarization at $\ell < 15$, measurements of polarization with $\ell > 15$ have steadily improved. The *Planck* team has shown excellent visual agreement between their best-fit ΛCDM model and their TE and EE polarization spectra for $\ell \geq 100$ but has not yet quantified the agreement (Planck Collaboration 2013c, Figure 11). On larger angular scales, $30 < \ell < 1000$, the CAPMAP (CAPMAP Collaboration 2008), QUAD (QUaD Collaboration 2009), QUIET (QUIET Collaboration 2012), and BICEP (BICEP1 Collaboration 2013) teams have shown, along with *WMAP* (Hinshaw et al. 2013), that the predicted E-mode signal is in quantitative agreement with the ΛCDM prediction. In addition, they placed limits on primordial and lensing B-modes. Through cross correlating the EB-reconstructed lensing signal with the Herschel-SPIRE maps, SPT (Hanson et al. 2013) demonstrated the presence of lensing B-mode polarization at 7.7σ. In a similar cross-correlation analysis, the POLARBEAR team found 2.3σ evidence (POLARBEAR Collaboration 2013) for lensing B-modes and also demonstrated the presence of lensed B-mode polarization through the EEEB and EBEB four-point functions at 4.2σ (POLARBEAR Collaboration 2014). Following that, POLARBEAR released their measurements of the TT, TE, and EE power spectra, 2σ evidence of non-zero BB power, and limits on the TB and EB spectra (POLARBEAR Collaboration 2014). Most recently, the BICEP2 team released their 7σ detection of degree angular-scale B-mode polarization along with a suite of related spectra (BICEP2 Collaboration 2014a).

This paper is the Atacama Cosmology Telescope (ACT) collaboration's first step in measuring CMB polarization and is organized as follows. In §2 we introduce the salient features of the instrument and then in §3 describe the observations and data reduction. In §4 we present our power spectra measurements and interpretation, and conclude in §5. For power spectra, we use the *Planck* notation: $\mathcal{D}_\ell^{\rm XY} = \ell(\ell+1)C_\ell^{\rm XY}/2\pi$ where XY ∈ TT, TE, TB, EE, EB, BB. We do not consider circular polarization (e.g., Alexander et al. 2009; Cooray et al. 2003). The maps are made in J2000 equatorial coordinates. We adopt the HEALPIX (Górski et al. 2005) convention for Stokes parameters Q and U. Polarization position angles respect the IAU convention (see, e.g., Hamaker & Bregman 1996), increasing from North towards East, and thus are computed as $\gamma_p = (1/2)\arg(Q - iU)$. We note that these are the same conventions adopted by *Planck* (see, e.g., Section 2.1 of Planck Collaboration 2014), although *Planck* uses Galactic coordinates.

2. THE INSTRUMENT

20771
[29] Department of Physics , West Chester University of Pennsylvania, West Chester, PA, USA 19383

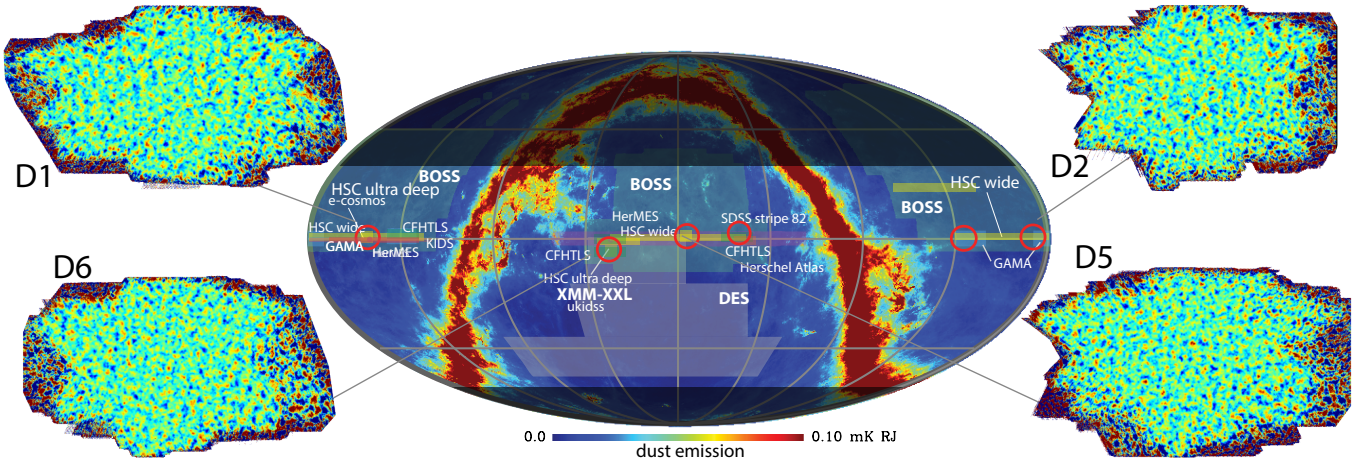

FIG. 1.— ACTPol maps and overlapping surveys. The maps have been filtered to emphasize $\ell > 300$. The power spectra are obtained with only the high S/N region of each map. Going from left to right across the equator, the red circles indicate patches D1, D6, D5, D4, D3 and D2 (the first ACTPol season focused on D1, D2, D5 and D6). More than half the sky, as indicated by the light colored area, is accessible to ACTPol. Overlapping surveys include SDSS (SDSS 2014), BOSS(BOSS 2014), CFHTLS (CFHTLens Collaboration 2013), XMM-XXL (XMM-XXL 2014), Herschel (HerMES & HeLMS, Oliver et al. (2012); Viero et al. (2014)), HSC (Subaru 2014), DES (DES 2014), GAMA (Driver et al. 2009), and KiDS (de Jong et al. 2013).

ACT is located at latitude 22°57′31″S and longitude 67°47′15″W at an altitude of 5190 m in Parque Astronómico Atacama in northern Chile. The 6 m primary mirror leads to arcminute resolution at millimeter wavelengths. A first-generation receiver, the Millimeter Bolometric Array Camera (MBAC; Fowler et al. 2007; Swetz et al. 2011), observed from Sept. 2007 through Dec. 2010. It was decommissioned and replaced by the polarization-sensitive ACTPol camera (Niemack et al. 2010) in 2013.

ACTPol is similar to MBAC in a number of ways: it has three separate "optics tubes" each of which terminates in an independent detector array; it uses three antireflection coated silicon lenses per tube to feed the detectors; it is located at the Gregorian focus of the telescope and illuminates the 2 m diameter secondary; the passbands are defined in part by free-space filters (Ade et al. 2006); IR radiation is blocked with free-space filters (Tucker & Ade 2006); and the transition-edge-sensor (TES) detectors are read out by time-division SQUID multiplexing (Chervenak et al. 1999), which is implemented using the Multi-Channel Electronics (MCE, Battistelli et al. 2008). ACTPol differs from MBAC in that the antireflection coating is achieved through a "metamaterial" (grooving of a silicon lens surface; Datta et al. 2013); cryogenic corrugated silicon horns feed two orthogonal polarizations (Britton et al. 2010; Hubmayr et al. 2012); the lower edge of the spectral passband is determined by the feed structure's input waveguide cutoff frequency, while the upper end is defined by free-space filters; the detector arrays (Grace et al. 2014; Pappas et al. 2014) are cooled to 100 mK as opposed to 300 mK; and a continuous dilution refrigerator cools the detector arrays instead of a ^{3}He sorption refrigerator, which enables daytime observations. The receiver is 40% larger than MBAC in volume.

Two of the optics tubes are designed to operate at 146 GHz and have 522 feeds (1044 TES detectors) each, 506 of which are typically used. In addition to the optical detectors, there are 6 dark detectors and 6 resistors for noise tests. The third tube will use a 90/146 GHz dichroic detector array with broad-band cold optics (Datta et al. 2014) and have 1020 TES detectors coupled to 255 feeds. For the results reported here, only one 146 GHz tube was installed. The second 146 GHz tube was installed in 2014 with the final tube scheduled for early 2015.

The array sensitivity (relative to the CMB) of the 2013 observations with the first optics tube is $\sim 19\,\mu\mathrm{K}\sqrt{\mathrm{s}}$. For comparison, the MBAC sensitivity at 148 GHz was $32\,\mu\mathrm{K}\sqrt{\mathrm{s}}$. The 405 most sensitive detectors provide 95% of the statistical weight in the maps, and the *in situ* median detector sensitivity is $340\,\mu\mathrm{K}\sqrt{\mathrm{s}}$ (Grace et al. 2014). Substantial improvements in sensitivity for 2014 observations are expected due to the unusually high precipitable water vapor (PWV) in 2013,[1] reductions in readout noise, reduced background loading, as well as the addition of new detector arrays.

The response of the ACTPol detectors diminishes with frequency such that it has a loading-dependent $f_{3\mathrm{dB}}$ (the frequency at 50% of the peak response) of 10-200Hz. When accounting for our scan speed and observing strategy, $f_{3\mathrm{dB}} = 70$ Hz corresponds to a rolloff in the angular power spectrum of 3% at $\ell = 3000$. The individual $f_{3\mathrm{dB}}$ frequencies of the detectors, including their dependence on loading from the changing elevation and precipitable water vapor (PWV), are accounted for in the analysis, although it contributes only a few percent (0.1% at $\ell = 3\,000$; 2% at $\ell = 10\,000$) difference in the power spectra compared to assuming the median value.

The passbands of the detectors were determined in the laboratory, before deployment, with a Fourier Transform Spectrometer. An effective frequency for the CMB $\nu_{\mathrm{CMB}} = 146 \pm 3$ GHz was measured and we adopt this throughout the analysis. The error bar is systematic, and will improve after planned measurements of the passband in the field. The resulting conversion between CMB and Rayleigh-Jeans equivalent source temperatures is $\delta T_{CMB}/\delta T_{RJ} = 1.66 \pm 0.04$. The Dicke bandwidth (Dicke 1946) is $\Delta\nu = 49$ GHz.

[1] The median nighttime PWV measured by the nearby Atacama Pathfinder Experiment weather monitor (APEX, Güsten et al. 2006) during the ACTPol 2013 season was 1.1 mm, while the median during the corresponding periods in 2008-2010 was 0.7 mm.

3. THE OBSERVATIONS AND DATA REDUCTION

3.1. *Sky coverage and scan strategy*

ACTPol data are acquired by scanning the telescope in azimuth at a variety of different elevations. A patch is scanned as it rises in the east and then again as it sets in the west. In this first year, we concentrated on four "deep fields" approximately centered on the celestial equator at right ascensions 150°, 175°, 355° and 35° which we call D1 ($73\,\mathrm{deg}^2$), D2 ($70\,\mathrm{deg}^2$), D5 ($70\,\mathrm{deg}^2$) and D6 ($63\,\mathrm{deg}^2$) respectively. The areas refer to the deep, rectangular regions with even coverage in the center of each patch that we use for power spectrum analysis. These patches were chosen for their overlap with other surveys and are shown in Figure 1. The separation of the patches is such that only one is visible at any given time, and in a typical 24 hour period all four patches were observed in sequence unless the observation would require the telescope to point within five degrees of the Sun. With our scan strategy, each patch is observed in a range of different parallactic angles while scanning horizontally. This is important for separating instrumental from celestial polarization and is a benefit of observing from a non-polar site.

The CMB fields are observed by scanning at 1.5°/s in azimuth, turning around in 1 s, scanning back to the original position, turning around in 1 s and repeating. The duration of the scan depends on elevation; a full cycle takes 16.4 s at an elevation of 35° and 20.9 s at 60°. This is done for 60 scans, or roughly 10 minutes, to form a time-ordered-data or "TOD" packet. The elevation is sometimes changed between 10 minute scans, at which point the detector bias is modulated to recalibrate and check for any changes in the time constants due to the change in sky load.

Data for the maps in Figure 1 were taken from Sept. 11, 2013 to Dec. 14, 2013. During this time, in addition to observing the CMB, we performed a number of systematic checks, characterized the instrument, observed planets, and observed the Crab Nebula (Tau A). The net amount of time that went into the maps was 236, 178, 311, and 305 hours for D1, D2, D5, D6 respectively. This represents 24%, 16%, 29% and 31% of the total CMB observation time. However, we use only the lowest noise regions of the maps, which constitute around 70% of the total observing time. This results in a white noise map sensitivity, in the sense of Figure 2 in Das et al. (2014), of 16.2, 17, 13.2, and 11.2 μK-arcmin respectively. For Stokes Q or U sensitivities these numbers should be multiplied by $\sqrt{2}$.

We divide the data into "day" (11:00-24:00 UTC) and "night" (0:00-11:00 UTC). The nighttime data fraction for patches D1, D2, D5 and D6 is 50%, 25%, 76% and 94% respectively. For this analysis we use only the nighttime data from D1, D5, and D6, amounting to 63% of the total.

3.2. *Beam, pointing, and polarization reconstruction*

We have found that multiple observations of planets (Hincks et al. 2010; Hasselfield et al. 2013) are essential for determining the beam profile. In 2013 Uranus was observed 120 times and analyzed as in Hasselfield et al. (2013). With all detectors combined, regardless of polarization, the beam is slightly elliptical with FWHM of $1.36'$ ($1.26'$) along the major (minor) axis. The solid angle is $\Omega_B = 194 \pm 6$ nsr ($2.29 \pm 0.07\,\mathrm{arcmin}^2$), before any smearing due to pointing. These results agree up to $\ell = 5000$ with a similar analysis of 20 observations of Saturn, a much brighter source. We did not detect any significant deviations when the data were split by the elevation of observation or whether the source was rising or setting. The beam profile was marginally detected in polarization maps of Uranus made in coordinates fixed to the optical system. Since the observations probed the planet at a range of parallactic orientations, this signal is interpreted as either I to P leakage in the optics or due to the analysis pipeline. The leakage from I to P due to this effect is less than 1.5% at $\ell < 5000$. The leakage is dominated by monopole terms and thus is highly suppressed in CMB maps because a range of parallactic angles is explored by the cross-linking scan strategy. Including the effects of cross-linking in the analysis of Uranus, we find the polarized fraction of the 146 GHz emission from Uranus to be less than 0.8% at 95% confidence.

A simple telescope pointing model is constrained using observations of planets at night. This model allows the pointing to be reconstructed with an rms error of $14''$. The impact of pointing variance on the full season CMB maps is handled as in Hasselfield et al. (2013), leading to effective beams in the CMB maps with solid angle $\Omega_B = 224 \pm 20$ nsr for D1, $\Omega_B = 234 \pm 14$ nsr for D5, and $\Omega_B = 224 \pm 12$ nsr for D6. The uncertainties include both beam and pointing contributions.

Average pointing error in the full season maps is assessed by comparing point source positions to the FIRST catalog (Becker et al. 1995; White et al. 1997). The absolute pointing error rms is found to be $5''$ in the nighttime maps, with no significant deviations when the data are split by elevation or time of observation. A $7''$ offset in the absolute pointing is uncorrected in this analysis.

Detectors co-located in the focal plane may point at slightly different positions on the sky, an effect seen by the BICEP2 Collaboration (2014b) at the $1'$ level. Because our detector pointing offsets are individually measured, and the map making procedure does not difference detectors directly (§3.4), this is not a primary concern for us but it is an important check of the instrument. From the analysis of planet observations, we find that the optical axes of a typical detector pair differ by less than $3''$.

During the day, the heat from the Sun distorts the telescope structure. The distortion pattern is repeatable, although we currently cut data between 17:00 and 20:00 UTC (13:00 and 16:00 local time) when the distortion is greatest. The distortion leads to two effects: the first is a pointing offset and the second is a repeatable deformation of the reflector, which changes the shape of the beam. Both of these effects lead to a roll-off in ℓ that resembles a low pass filter and can be treated as a beam effect in the likelihood. We do not include the daytime data in our cosmological parameter analysis, as models for the daytime beam response are still in development. Nevertheless, our preliminary treatment of the daytime beam produces power spectra that are consistent with nighttime spectra (Figure 5) and pass null tests (see §4.1).

Each detector is sensitive to a single linear polariza-

tion direction, and the relative angles of the detectors within each array are set by lithography during fabrication. The optical detector orientations are calculated by raytracing through the full optical system to determine the projection of each detector within an array on the sky.

CMB temperature fluctuation measurements from *Planck* and *WMAP* are used to calibrate the ACTPol T, Q, and U maps with a common rescaling factor, as described in §4. However, signal in the Q and U maps will be attenuated by an additional factor $\alpha_{\rm P}$, which is different from unity due primarily to errors in the assumed detector polarization angles. For the present analysis we take $\alpha_{\rm P} = 0.95 \pm 0.05$; this is discussed further in §3.3.

Any mean offset between the assumed and actual detector polarization angles must be understood in order to properly decompose polarized intensity into E and B components. The polarized CMB may be used to assess the offset angle under the assumption that the intrinsic correlation between the E and B signals is zero. Systematic optical effects associated with polarization, including parallactic rotations, cause a leakage from E to B modes and induce spurious signal in EB and TB correlations (e.g., Shimon et al. 2008). The most likely instrument polarization reference angle may thus be determined by minimizing the inferred EB signal with respect to offset angle (e.g., Keating et al. 2013). Under these assumptions, the ACTPol E and B spectra from $500 < \ell < 2000$ constrain the instrumental polarization offset angle to be $\delta\gamma_p = -0.2^\circ \pm 0.5^\circ$. This result is referred to as the EB-nulling offset angle. Since this angle is small and consistent with zero, we do not correct the spectra for this effect in the present analysis. The agreement with zero suggests that the optical modeling procedure is free of systematic errors at the 0.5° level or better.

Naturally, estimating the polarization offset angle by assuming E and B to be uncorrelated eliminates sensitivity to models, such as isotropic cosmic birefringence, where the distinguishing characteristic is a constant EB cross-correlation. As an alternative calibration approach, measurements of the polarized signal from a bright astrophysical source may be compared to values from the literature. The Crab Nebula is a convenient source for this purpose.

3.3. *The Crab Nebula*

The Crab Nebula, or Tau A, is an extended polarized supernova remnant whose emission below ≈ 1 THz is dominated by synchrotron radiation (see, e.g., Hester 2008). Its brightness and compactness provide a convenient polarization reference for millimeter-wavelength observatories. From *WMAP* measurements at 93 GHz, Tau A is polarized in the direction $\gamma_p = 148.9^\circ \pm 1.8^\circ$ in equatorial coordinates (Weiland et al. 2011). These agree with the IRAM observations at 89.2 GHz which give the direction as $\gamma_p = 149.9^\circ \pm 0.2^\circ$ when smoothed to a 5′ Gaussian beam (Aumont et al. 2010).

Tau A was observed roughly every second day during the 2013 observing season. A co-added map from a subset of these observations is shown in Figure 2. The results presented here are a preliminary analysis with the goal of demonstrating the level to which the polarization sensitivity of the instrument is understood.

Because of their 27″ resolution and higher precision, we take the IRAM results as our reference. We downgrade the resolution of the ACTPol maps to match a 5′ Gaussian beam and compare to the Aumont et al. (2010) values for this case.[2] The difference corresponds to an instrument polarization offset angle of $\delta\gamma_p = -1.2^\circ \pm 0.2^\circ$ at the pulsar position in the smoothed maps, where the uncertainty is statistical and is assessed by comparing three independent sets of ACTPol observations.

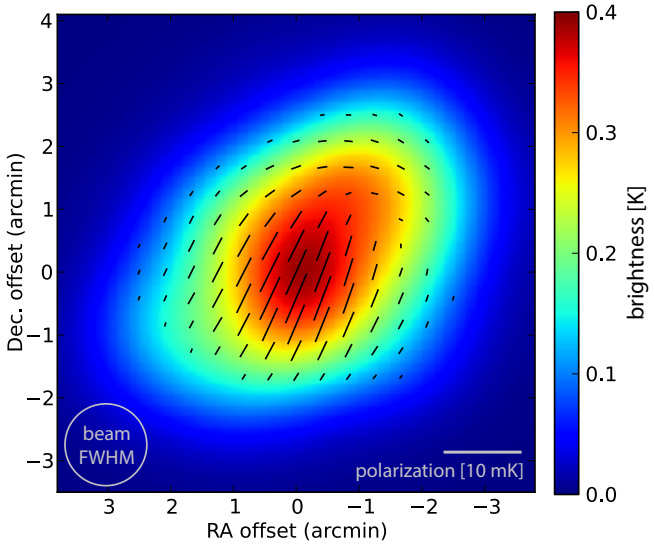

FIG. 2.— ACTPol intensity and polarization map of the Crab Nebula (Tau A). The brightness scale is in differential temperature units, relative to the CMB at 146 GHz (for Rayleigh-Jeans brightness temperature, divide by 1.66). Black bars show polarization direction, with length proportional to polarized intensity ($(Q^2 + U^2)^{1/2}$), which reaches a maximum of 6.8 mK. The origin of the coordinate system corresponds to the Crab Pulsar position. Note the variation in polarization angle and fraction across the source, which complicates the use of the source as a precision calibrator. Polarization features are in good qualitative agreement with the higher resolution, 89.2 GHz maps of Aumont et al. (2010); a numerical comparison is discussed in the text. This map has been resampled to 2″ pixels from its original 30″ resolution but has not otherwise been smoothed.

The analysis of Tau A was performed while keeping the EB result "blinded," and provides an independent probe of the instrumental polarization offset angle. With the EB result unblinded, the difference between the IRAM-based and EB-nulling polarization offset angles is 1.0° ± 0.5°. This difference is consistent with the 1.1° ± 0.5° offset found by POLARBEAR Collaboration (2014) at 150 GHz, and increases the evidence of a ≈ 1° difference in Tau A polarization between 90 and 150 GHz. (The uncertainty stated here for the POLARBEAR result does not include a contribution from IRAM overall polarization uncertainty.)

Studies of the total flux density of the nebula have shown that the spectrum is well described by a single synchrotron component (Macías-Pérez et al. 2010), and predict negligible variations in polarization fraction and angle at 150 GHz. However, high resolution studies of the source at 150 GHz and 1.4 GHz demonstrate non-negligible variations of the spectral index over the surface of the source (Arendt et al. 2011). Since the polarization

[2] We are collaborating with the *Planck* team to develop Tau A as a standard but this present analysis used only public IRAM results.

angle also varies over the source, the total polarized flux and mean polarization angle may have a non-trivial behavior as a function of frequency.

Our understanding of the polarization efficiency is currently limited by uncertainty in individual detector polarization angles. Comparison of individual detector timestreams to the ACTPol Tau A maps provides limits on these angle errors. At the present time we can only conclude that the polarization efficiency $\alpha_{\rm P}$ is at least 0.9, corresponding to an rms uncertainty in the polarization angles of 10°. While this is somewhat larger than the expected deviations, for the present analysis we consider the full range $0.9 < \alpha_{\rm P} < 1.0$. In the cosmological likelihood analysis, the efficiency is given a uniform prior over this interval. When stating polarization fractions below, we simply take $\alpha_{\rm P} = 0.95 \pm 0.05$ and treat the error as Gaussian.

For the purposes of stating our measurements of the Tau A polarization signature, we apply the EB-nulling instrumental polarization offset. These results apply at 146 GHz, for an instrument with a $5'$ Gaussian beam. At the pulsar position, the polarization fraction is $(9.2 \pm 0.5)\%$ and the polarization angle is $150.9° \pm 0.5°$ East of North. At the peak of the smoothed intensity (which lies $22''$ northwest of the pulsar position), the polarization fraction is $(8.7 \pm 0.4)\%$ at an angle of $150.7° \pm 0.6°$.

3.4. *Data selection and pre-processing*

The data selection closely follows the path laid out in Dünner et al. (2013). The main difference in the TOD processing is the procedure for calibrating each detector, as a larger fraction of the detectors are operating near the saturation level. A set of reliable detectors is used to determine an absolute calibration level that is stable over variations in detector temperature and loading. A low-order polynomial is removed from each time stream to limit the impact of low frequency drifts. Then a per-TOD flat-fielding is performed on all the detectors, using the common-mode signal from the atmosphere. At this point the properties of the detector time streams are characterized and screened. The output of this step in the pipeline, which we call the cuts package, is a list of science grade detectors with $f_{\rm 3dB} > 20$Hz, well-behaved noise, and a common relative calibration. In addition, we reject data when the PWV> 3 mm. Note that the polarization orientation of a detector does not enter into the data selection or flat-fielding. The time stream processing (such as polynomial removal) used to determine the cuts and calibration are not the same as those applied to the data during mapmaking.

3.5. *Map making*

After applying the cuts, the time-ordered data are projected on the sky by solving the maximum-likelihood map making equation for a vector of map pixels $\mathbf{m}$,

$$A^T N^{-1} A\mathbf{m} = A^T N^{-1}\mathbf{d}, \qquad (1)$$

via the preconditioned[3] Conjugate Gradients algorithm. Here $\mathbf{d}$ is the set of time-ordered data, N is the noise covariance of $\mathbf{d}$ and A is the generalized pointing matrix that projects from map domain to time domain. This follows the method used in Dünner et al. (2013), but extends it to polarization. Polarization is handled by including each detector's response to the I, Q and U Stokes parameters in the pointing matrix, so the analysis does not depend on explicit detector pair differencing. This approach, coupled with the parallactic angle coverage of our scan strategy, naturally suppresses monopole and dipole polarization leakages. The different noise properties for temperature and polarization are represented as detector correlations in the noise covariance matrix, which we model as stationary in 10 minute chunks and measure from the data.[4] To avoid bias from applying the noise model to the same data it is measured from, we make a second pass where the estimated sky map is subtracted from the time-ordered data before the noise model is reestimated.

In principle, maximum-likelihood map making results in unbiased, minimum-variance sky maps. But there are a few caveats. With the Conjugate Gradients technique, the number of steps needed to solve for each eigenmode depends on its eigenvalue, and some degenerate or almost degenerate modes never converge. The nature of the degenerate modes depends on the patch size and scanning pattern, but in the present analysis they correspond to the low signal-to-noise modes at multipoles $l \lesssim 50$. Additionally, our current treatment of ground pickup results in a bias on these large scales (see §3.6).

With our current data set, each 70 deg^2 map is a reduction of $\sim 10^{11}$ samples into $\sim 10^6$ pixels, making this the most computationally intensive step in the analysis. Nevertheless, due to the short observation time so far, the costs are still relatively modest compared to the original ACT analysis. Figure 3 shows an example map from patch D6. For display purposes, a bandpass filter has been applied to maximize signal-to-noise. Example difference maps (odd vs. even pairs of nights) for the same region are shown in Figure 4.

3.6. *Ground, lunar, and solar pickup*

ACT has two levels of ground screens. One screen is fixed to the telescope and scans with it. This entire system sits inside a second 13 m high fixed ground screen. Nevertheless, we still detect a spurious signal which we interpret as ground pickup. When the telescope points to the northeast between azimuths $\sim 25° - 85°$ we observe a spurious signal with a $\sim 30°$ period in azimuth, with little elevation dependence, and a peak-to-peak amplitude of $\sim 200\mu$K in Q and U. This is consistent with signal from the nearby mountain Cerro Toco being diffracted over the top of the ground screen's 30° wide panels. While this signal is washed out when projected on the sky, it would still be a contaminant of $\pm 20\mu$K or more in our polarization maps if ignored.

The ground signal can be disentangled from the sky because it is constant in azimuth during a scan and does not rotate with parallactic angle like the sky. The exceptions are modes on the sky that depend only on declination, not right ascension (such as the spherical harmonics with $m = 0$). These show up as pure functions of

[3] We currently use a simple binned preconditioner, with a 3x3 matrix at each (I, Q, U) map pixel that inverts the (polarized) hit-count map. We are investigating other approaches such as a stationary correlation preconditioner (Næss & Louis 2013).

[4] In temperature, the atmosphere is our largest noise term for $\ell \lesssim 3\,000$, but atmospheric noise is almost absent in polarization.

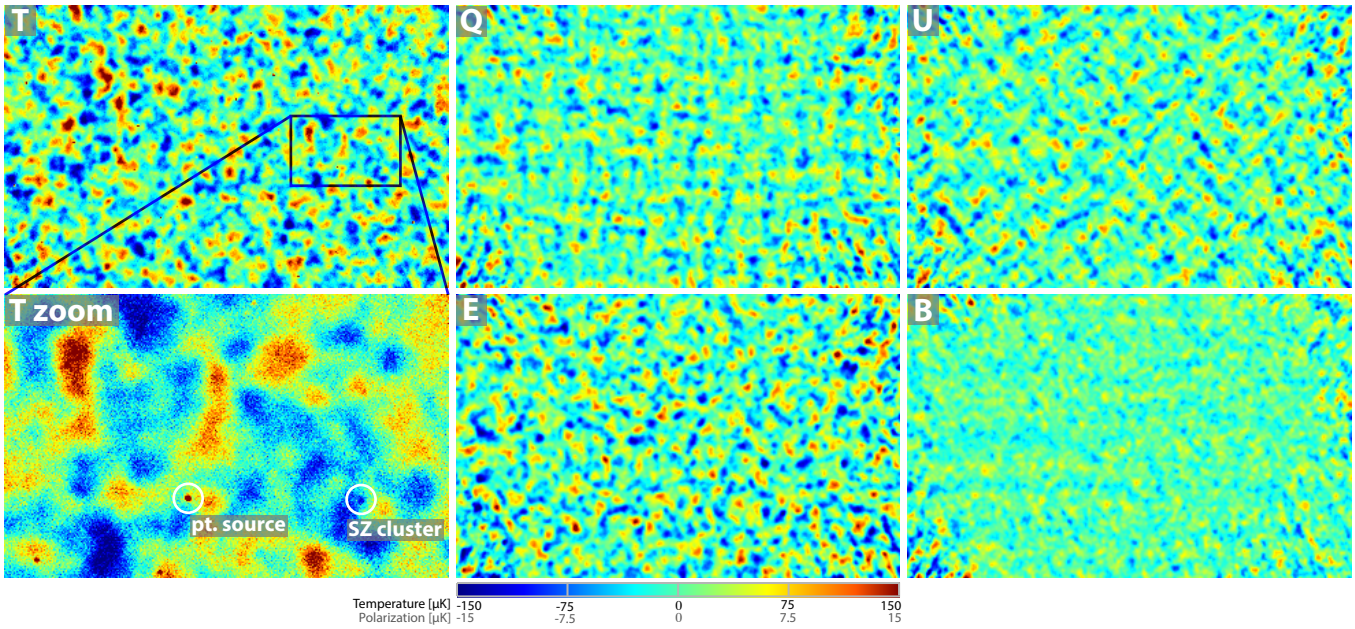

FIG. 3.— Example maps from the region $29.65° < \mathrm{RA} < 40.49°$ (horizontal), $-7.60° < \mathrm{Dec} < -0.68°$ (vertical), in the center of patch D6. Panels 1,2,3,5,6 (left to right, top to bottom) show T, Q, U, E and B respectively. Panel 4 is a zoom on a $2.79° \times 1.73°$ subregion of the T map, showing the full map resolution. The maps have been bandpass filtered to maximize signal-to-noise ($240 < \ell$ for temperature, $260 < \ell < 1370$ for polarization). The visible patterns in the Q and U maps are consistent with a sky dominated by E-mode polarization, as can be seen in the derived E and B maps. The B map is consistent with noise except for a faint $m = 0$ (constant declination) ground residual (see §3.6). We do not use $m = 0$ modes in the power spectrum estimation. See Figure 4 for an illustration of the noise properties in these filtered maps. The circled galaxy cluster candidate, ACT-CL J0205.2-0439, is within $2'$ of a CFHTLS cluster candidate with photometric redshift $z = 1.1$ (Durret et al. 2011) and three concordant galaxies with spectroscopic $z = 0.97$ found in the VIMOS Public Extragalactic Survey (Garilli et al. 2014). The circled point source may be associated with FBQS J0209-0438, a quasar at $z = 1.128$ (Véron-Cetty & Véron 2006).

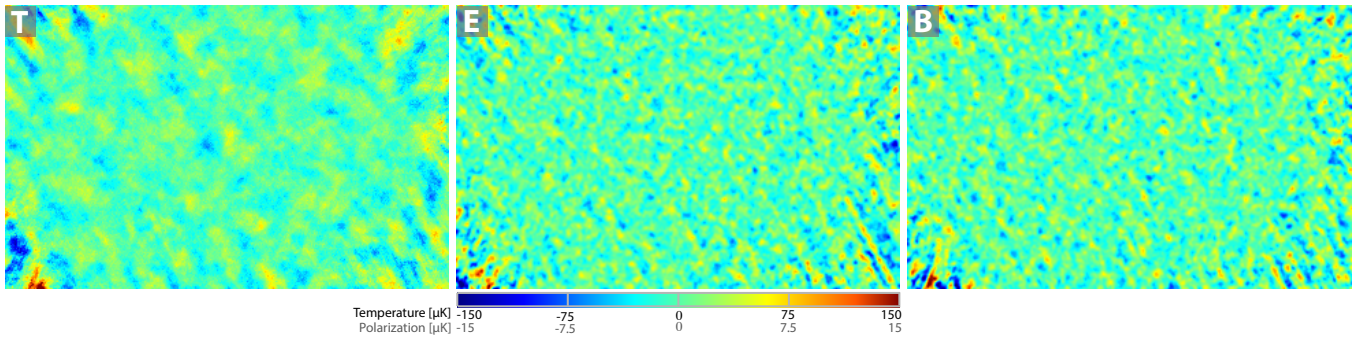

FIG. 4.— Difference maps (odd vs. even pairs of nights) for the same region as Figure 3, illustrating the noise properties of the map. Correlated noise is visible as diagonal stripes aligned with our dominant scanning directions (diagonally in these coordinates). These are the map-space equivalent of the correlated noise in the time-ordered data. Noise correlations are taken into account in the noise model in the power spectrum estimation.

azimuth during a constant elevation scan, and are degenerate with the ground even when observing at multiple azimuths and elevations. The remaining modes could, in principle, be disentangled, but in the current analysis we remove both these and the degenerate modes by applying an azimuth filter to the time-ordered data and excluding Fourier modes with $|\ell_y| < 50$ from the power spectrum estimation.[5]

While the filters are effective at suppressing the ground pickup, they also remove some bona fide sky signal, making our maps and power spectra slightly biased. The effects of the filtering are assessed by passing simulated maps of the polarized CMB through the filtering procedure, and comparing the power spectra of the input and output maps. The main effect of the filter is to suppress, slightly, the signal in temperature (polarization) on large angular scales, with a transfer function that decreases from 0.995 (0.99) at $\ell = 500$ to 0.95 (0.9) at $\ell = 200$. Leakage from E to B is also seen, but at a level that is negligible for this analysis. Our simulations show that with a more sophisticated treatment we can expect a significantly reduced impact from ground signals in future ACTPol results.

We investigate the possibility of contamination from sidelobes overlapping the Sun or Moon by making maps in coordinates centered on these objects. We identify two sidelobes this way, one around 20° away from the boresight, and another one 120° away. These have an

[5] Excluding $|\ell_y| < 50$ removes an approximately $4\mu\mathrm{K}/°$ residual ground gradient from the azimuth-filtered maps.

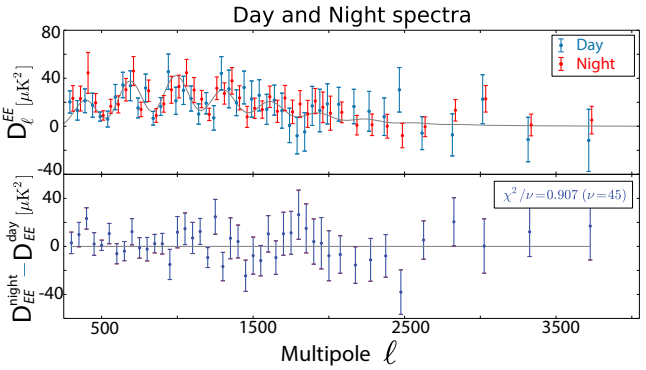

FIG. 5.— The D1 day and nighttime EE spectra (top), and their difference (bottom); they are consistent.

amplitude of around 200μK in polarization for the Sun, but are not detected for the Moon. Based on this, we cut all scans that hit these regions in Sun-relative coordinates. As a precautionary measure, we also cut all scans within 10° of the Moon, which results in a negligible loss of data.

4. THE POWER SPECTRA AND INTERPRETATION

We compute the temperature and polarization power spectra of the maps following the methods described in Louis et al. (2013), which builds on those used in Das et al. (2011, 2014). The code was checked extensively with simulations and is able to extract an E/B mode power spectrum signal to within 0.1σ in maps with 5 μK noise in the presence of uneven weights across the maps, irregular boundaries, and cutouts for sources.

In this analysis we use $\ell_{\rm min}^{\rm TT} = 500, \ell_{\rm min}^{\rm TE,EE} = 250$, and $\ell_{\rm max}^{\rm TT,TE,EE} = 9\,000$.[6] In two-dimensional Fourier space we mask a vertical strip with $|\ell_x| < 90$ (as in Das et al. 2011, 2014), and a horizontal strip with $|\ell_y| < 50$, as described in §3.6. The maps are calibrated to the *Planck* 143 GHz temperature map (Planck Collaboration 2013a) following the method in Louis et al. (2014), resulting in a 2% uncertainty. The overall calibration measured by *Planck* and *WMAP* disagree (Planck Collaboration 2013c), so we then multiply all maps by a factor of 1.012 to correspond to the more mature *WMAP* calibration. As described in §3.3, the polarization maps are assumed to have an additional 5% calibration uncertainty.

We test the parameter extraction and power spectrum pipeline as follows. We generate a simulated[7] sky in temperature and polarization with the *WMAP*+ACT parameter set Calabrese et al. (2013)[8] and with a realistic level of unresolved point source power, extract the portion corresponding to the ACTPol coverage for each patch, and add a realization of the full inhomogeneous noise model as measured. We then take the power spectra of the maps, and from the power spectra derive cosmological parameters, marginalizing over foreground parameters. We run this process 100 times and recover the input cosmology to within 0.1σ. We use the simulations to construct the covariance matrix for the data.

In this analysis we do not account for cosmic aberration (Jeong et al. 2014), super sample lensing (Manzotti et al. 2014), or the effect of the flat-sky approximation. We have simulated these sub-dominant effects and find that they have a negligible impact on derived ΛCDM cosmological parameters; however, we are extending our pipeline to account for them in future ACTPol analysis.

TABLE 1
NULL TESTS

Test	Patch	Spectrum	χ^2/dof	P.T.E
Detector	D5	TT	0.92	0.65
		EE	1.51	0.01
		TE	0.65	0.98
	D6	TT	1.39	0.03
		EE	0.91	0.66
		TE	1.02	0.43
Turnaround[a]	D5	TT	0.76	0.91
		EE	0.71	0.95
		TE	0.86	0.76
	D6	TT	0.92	0.65
		EE	1.18	0.17
		TE	0.76	0.91
Splits[a]	D5	TT	0.67	0.97
		EE	0.72	0.94
		TE	0.55	0.997
	D6	TT	0.94	0.60
		EE	0.77	0.89
		TE	0.77	0.89
	D1	TT	1.60	0.003
		EE	0.77	0.89
		TE	1.14	0.23
Patches	D1-D5	TT	0.89	0.70
		EE	0.89	0.70
		TE	1.24	0.11
	D1-D6	TT	0.67	0.97
		EE	0.66	0.97
		TE	1.26	0.09
	D5-D6	TT	0.94	0.60
		EE	0.94	0.60
		TE	0.96	0.56
Day-Night	$D1^N$-$D1^D$	EE	0.91	0.64

[a]Reported for $(s_0^t - s_1^{nt}) \times (s_2^t - s_3^{nt})$ for the turnaround nulls, and $(s_0 - s_1) \times (s_2 - s_3)$ for the split nulls. The other permutations are reported in Table 2.

4.1. *Null tests*

We perform a set of null tests similar to those done for the ACT temperature analysis (Das et al. 2014): compare the data with and without telescope turnaround periods incorporated,[9] compare the results from different detector sets, and compare the maps made from the four different time-splits.[10]

For the detector null, we split the array in half by those most likely to have a different calibration and polarization response, and make two split maps for each subset.

[6] We use a larger value of ℓ_{min} for TT because atmosphere $1/f$ modes impact the T maps much more than the polarization maps.

[7] To include the effects of our flat-sky approximation in our simulations, each simulated map is generated on the full, curved sky and then projected to our native cylindrical equal-area maps.

[8] Throughout this work, the WMAP+ACT parameters differ slightly from the results of Calabrese et al. (2013) as a result of incorporating the finalized ACT beam window functions (Hasselfield et al. 2013).

[9] Labeled s^t and s^{nt} respectively.

[10] s_i for i from 0 to 3, such that $s_i = \{j : i = j \mod 4\}$, where $\{j\}$ is the set of all observations in chronological order, i.e. a 4-way equivalent of an odd-even split.

TABLE 2
SPLIT AND TURNAROUND NULLS

Patch	Combination	Spec.	χ^2/dof Splits	P.T.E	χ^2/dof Turn.[a]	P.T.E
D5	$(s_0 - s_2) \times$	TT	0.65	0.98	0.64	0.98
	$(s_1 - s_3)$	EE	0.88	0.72	0.86	0.77
		TE	0.77	0.90	0.76	0.90
	$(s_0 - s_3) \times$	TT	1.08	0.31	1.09	0.31
	$(s_1 - s_2)$	EE	0.92	0.64	0.95	0.58
		TE	1.21	0.14	1.34	0.05
D6	$(s_0 - s_2) \times$	TT	0.93	0.61	1.17	0.19
	$(s_1 - s_3)$	EE	0.60	0.99	0.75	0.92
		TE	0.72	0.94	0.79	0.87
	$(s_0 - s_3) \times$	TT	0.96	0.55	1.06	0.36
	$(s_1 - s_2)$	EE	0.74	0.92	1.06	0.35
		TE	0.91	0.67	1.01	0.46
D1	$(s_0 - s_2) \times$	TT	0.68	0.97		
	$(s_1 - s_3)$	EE	0.89	0.71		
		TE	1.16	0.20		
	$(s_0 - s_3) \times$	TT	0.92	0.65		
	$(s_1 - s_2)$	EE	0.69	0.96		
		TE	1.30	0.06		

[a]For turnarounds the second split-map in each difference has the turnaround removed, e.g., the first row has $(s_0^t - s_2^{nt}) \times (s_1^t - s_3^{nt})$.

We form the difference map between detector sets for each split and then compute their cross-spectrum. For the turnaround null we test for effects generated by the acceleration of the telescope. As in Das et al. (2014) we make four split maps with the turnaround data removed, cutting 12-13% of the data, and form a set of difference maps between splits with and without turnarounds. We apply these tests to the D5 and D6 patches, which have the deepest coverage.

We have also compared the daytime and nighttime spectra for the D1 patch, and find them to be consistent (see Figure 5). The null tests are summarized in Table 1, and Table 2 shows the other permutations of the null spectra for the turnaround excision and split nulls.

An assessment of the consistency of the χ^2 and probability-to-exceed (PTE) statistics is complicated by the fact that the many tests probe the same noise realization and are thus correlated. For independent measurements, the distribution of PTE values should be consistent with a uniform distribution. Our distribution of PTE values is somewhat skewed towards values greater than 0.5. However, there is no systematic failure of the χ^2 test in these results, and the most extreme values of 0.003 and 0.997 are not statistically surprising for a sample of this size. The lowest PTE is for a D1 TT split null (0.003), and the highest for a D5 TE split null (0.997), but the other permutations of these null spectra, shown in Table 2, do not show outlier behavior.

The different patches have different coverage, are observed at different times, have different (but low) levels of potential Galactic contamination, and are observed differently relative to the local environment. For the analysis of many systematic effects, they are effectively independent measurements, so the spectra can be compared as an additional test. Figure 6 shows the combined power spectra from the three patches. For the spectra where a signal is detected (TT, TE, EE) we have subtracted the *WMAP*+ACT best-fit model (Calabrese et al. 2013, reproduced from) and show the residuals. For reference we show the small difference between the *WMAP*+ACT model and the Planck+WP+highL model for TT, TE and EE. For TB, EB, and BB we just show the data. The measured BB signal is consistent with zero as expected with the current ACTPol sensitivity. We find that the spectra are consistent among patches, with the χ^2 of their differences given in Table 1 for TT, TE, and EE.

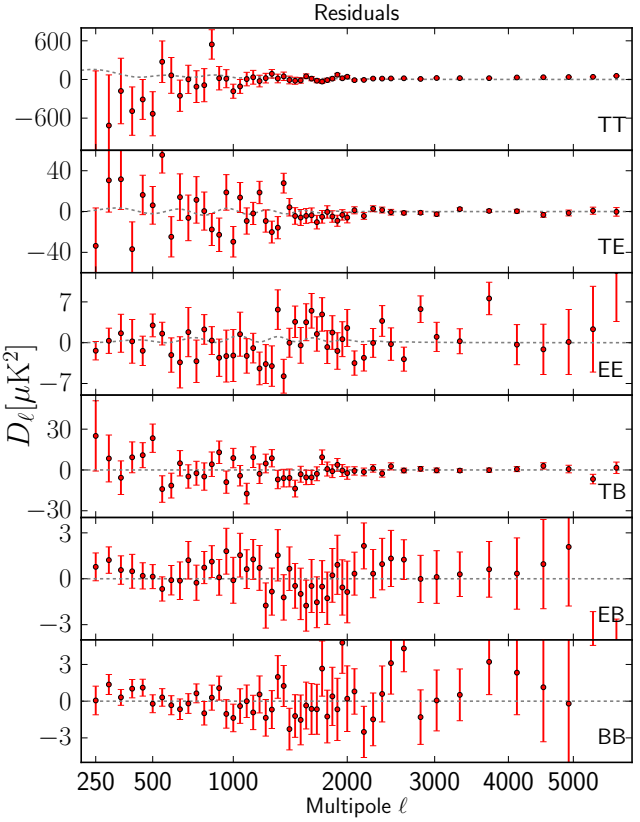

FIG. 6.— Residuals of measured power spectra relative to the *WMAP*+ACT best-fit model (for which TB, EB, and BB are assumed to be zero). Dashed curve shows the small difference between the *WMAP*+ACT and Planck+WP+highL best-fit models. The x-axis is scaled as $\ell^{0.5}$.

4.2. *Foreground emission*

We test for foreground emission in the temperature maps by correlating the ACTPol maps with the FDS dust template map (Finkbeiner et al. 1999). The dust level in this template has been shown to be consistent with the *Planck* 353 GHz maps (Planck Collaboration 2013b) at the 30% level. The predicted contribution of dust to the temperature anisotropy power spectrum is measurable but small, less than 2 μK^2 at $\ell = 2000$ as shown in Figure 7. We do not correct for it in the maps or likelihood at this stage.

Based on the recent results from *Planck* (Planck Collaboration 2014), the polarization fraction in D1, D5, and D6 is roughly 5%. We take 10% as an upper limit and thus the contribution from polarized dust emission to the power spectrum is expected to be less than 0.02 μK^2 at $\ell = 2000$. The contribution from polarized synchrotron emission is expected to be at this level or smaller. A full analysis must await the public release of the *Planck* polarization maps. However, the consistency shown in Table 1 between patches D1, D5, and D6, each with dif-

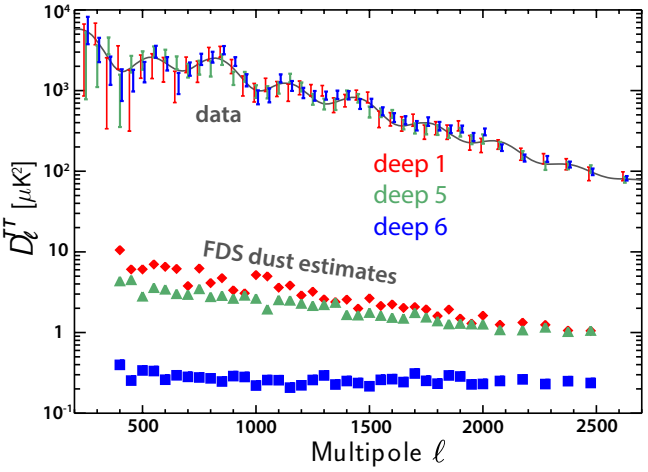

FIG. 7.— The expected temperature power spectrum of thermal dust in the ACTPol patches, estimated using the Finkbeiner et al. (1999, FDS) template, plotted below the ACTPol temperature power spectra. The dust amplitude is ≤ 2 μK^2 at $\ell = 2000$ ($\sim 1\%$ of the TT spectrum amplitude, or 10% in the maps). We show that the FDS template is a good tracer of the sub-dominant dust component by correlating it with the ACTPol maps, finding a cross-correlation consistent with unity to within 1σ.

TABLE 3
REBINNED BB POWER SPECTRUM, $\mathcal{D}_\ell = \ell(\ell+1)C_\ell/2\pi$ (μK^2), SHOWN IN FIGURE 12.

ℓ	ℓ range	BB	
		$\mathcal{D}_\ell$	$\sigma(\mathcal{D}_\ell)$
650	225 – 1075	0.20	0.21
1550	1075 – 2025	-0.18	0.41
2575	2025 – 3125	0.52	0.77
4325	3125 – 5525	1.87	1.35

ferent foreground levels, suggests that any possible contribution is small compared to the cosmological polarization signal.

4.3. *TT,TE,EE,BB*

Figure 8 shows the combined ACTPol TT and EE spectra along with independent data sets from ACT temperature measurements and *Planck*. The full TT/TE/EE set is shown in Figure 9. The TE spectrum is shown in Figure 10, together with results from other CMB polarization experiments. These and the spectra from Figure 6 are presented in Table 6. The bandpowers are not significantly correlated, and bandpower window functions are computed as in Das et al. (2014) to compare theory models to these data. Figure 11 shows the EE spectrum on a linear scale, and Figure 12 shows the BB spectrum rebinned into 4 bins based on the numbers in Table 3. Rebinning to wider bins increases the signal-to-noise ratio at the cost of resolution.

We observe six acoustic peaks in the EE power spectrum, out of phase with the TT spectrum as expected in the standard cosmological model, and six peak/troughs in the TE cross-correlation. We detect no significant BB power.

As a simple test, we find the χ^2 for the ACTPol EE data compared to the ΛCDM 6-parameter model using a) the *WMAP*+ACT parameters (Calabrese et al. 2013), and b) the *Planck* best-fit parameters (Planck Collaboration 2013c). The reduced χ^2 values for the two models are 1.09 and 1.12 respectively with 55 dof and no free parameters (with PTE of 0.30 and 0.25). For the TE data the reduced χ^2 for the two models are 1.26 and 1.24, again with 55 dof and no free parameters (PTE of 0.09 and 0.18).

TABLE 4
COMPARISON OF COSMOLOGICAL PARAMETERS AND 68% CONFIDENCE INTERVALS FOR DIFFERENT DATA SETS.

	WMAP+ACT[a]	Planck[b]	ACTPol TE,EE[c]
$100\Omega_b h^2$	2.247 ± 0.041	2.207 ± 0.027	2.073 ± 0.135
$\Omega_c h^2$	0.1143 ± 0.0044	0.1198 ± 0.0026	0.131 ± 0.015
$10^4\theta_A$	103.95 ± 0.19	104.132 ± 0.063	104.12 ± 0.31
$\ln(10^{10}A_s)$	3.094 ± 0.041	3.090 ± 0.025	3.190 ± 0.085
n_s	0.970 ± 0.011	0.9585 ± 0.0070	[0.970 ± 0.011]
τ	0.089 ± 0.013	0.091 ± 0.0135	[0.089 ± 0.013]
Derived[d]			
σ_8	0.830 ± 0.021	0.828 ± 0.012	0.933 ± 0.064
H_0	69.7 ± 2.0	67.3 ± 1.2	63.2 ± 5.5

[a]Joint analysis of *WMAP*+ACT as described in the text, assuming massless neutrinos.
[b]Parameters from 'Planck+WP+highL' Planck Collaboration (2013c), assuming a 0.06 eV summed neutrino mass.
[c]Parameters use just ACTPol TE and EE data, with priors imposed on τ and n_s from *WMAP*+ACT (given in brackets) and assuming massless neutrinos.
[d]The derived parameters σ_8 and H_0 (in units of km s^{-1} Mpc^{-1}) are also presented.

4.3.1. Λ*CDM*

Another test of the standard ΛCDM cosmological model is to fit its parameters from just the ACTPol EE and TE data. In this combination, *WMAP* is used to put a prior on the optical depth and scalar spectral index, since ACTPol does not measure the largest angular scales. We estimate parameters using standard methods as in Sievers et al. (2013) and Calabrese et al. (2013), and marginalize over Poisson source powers for the TE and EE spectra. Other foregrounds are assumed to be unpolarized.

The results are reported in Table 4 and shown in Figure 13 for the physical baryon density, $\Omega_b h^2$, the physical cold dark matter density, $\Omega_c h^2$, the acoustic scale θ_A, and the amplitude of primordial curvature perturbations, A_s, defined at pivot scale $k_0 = 0.05$ Mpc^{-1}. The polarization data are in excellent agreement with the standard model constrained by the *Planck* temperature data (Planck Collaboration 2013c).

We repeat the same test with just the ACTPol TT data, including the foreground model as in Dunkley et al. (2013) to account for Poisson and clustered point sources and the thermal and kinematic Sunyaev-Zel'dovich effects. The parameters are consistent with the ACTPol TE/EE results, but more weakly constrain the acoustic scale and the physical baryon and CDM densities (see Figure 13). This highlights the potential of the E-mode polarization signal for cosmological constraints (see e.g., Galli et al. 2014), with sharper acoustic features and less contamination from atmosphere and foregrounds. At this stage of measurement, however, the polarization data are not as precise as the *Planck* or *WMAP* temperature data primarily because they are taken over a relatively small region of sky. Parameter constraints from ACTPol combined with *Planck* are currently dominated by the temperature data.

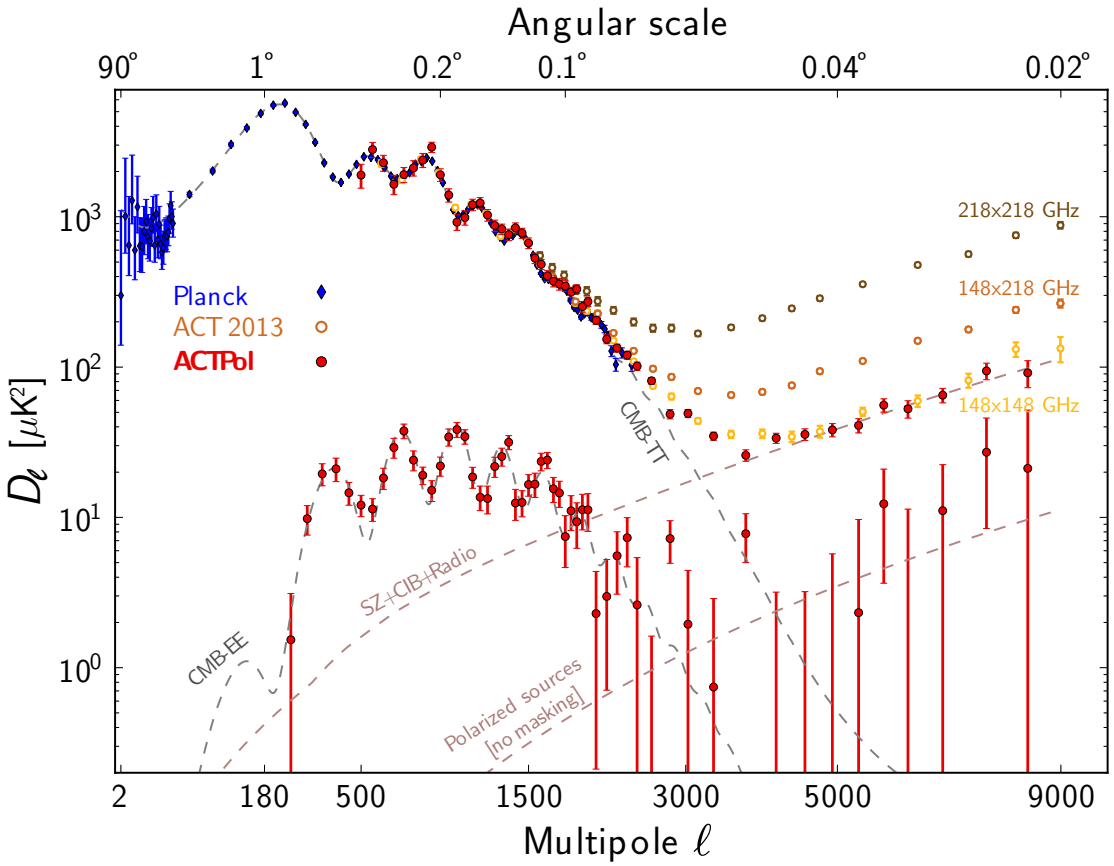

FIG. 8.— The *Planck*, ACT, and ACTPol data. Many *Planck* points for TT are obscured by the ACT data for $1000 < \ell < 2500$. The model spectra labeled CMB-TT and CMB-EE are for 'Planck+WP+highL' (Planck Collaboration 2013c). It is clear that the same model is an excellent fit to the TT and EE data (see §4.3.1). Recently *WMAP* (Bennett et al. 2013) and SPT (Story et al. 2013) have also published new data on the TT spectrum in this range, which are not shown here. All measurements are broadly consistent. The best-fitting Poisson polarized source level is shown, with no sources masked. A non-zero level is preferred, but the distribution is consistent with zero at 95% confidence, with $a_p^{\rm pol} < 2.4$. The x-axis is scaled as $\ell^{0.45}$ to emphasize the mid-ℓ range.

4.3.2. *Peak/Dip Phases*

ΛCDM predicts that the TT and polarization peaks should be out of phase. We test this quantitatively, in a manner similar to that used in Readhead et al. (2004). We start by computing the theoretical ΛCDM TE and EE power spectra based on the best-fit parameters from Section 4.3.1. Since we wish to test for any unexpected phase shift between the TE and EE spectra, we construct a simple parametric model that approximates the ΛCDM spectra, but has individually adjustable phases for each spectrum. This model takes the form $r_1(\ell)+r_2(\ell)\cos(2\pi\ell/L+\phi)$ where $r_1(\ell)$ and $r_2(\ell)$ are rational functions with third-order polynomials in both the numerator and denominator, L is the period of the peaks, and ϕ is the phase of the pattern, all of which are fit independently to each spectrum such that the deviation from the ΛCDM spectra is minimized in the range $100 < \ell < 2000$. The result is best-fit rational functions $\hat{r}_1(\ell)$ and $\hat{r}_2(\ell)$ and a best-fit phase parameter $\hat{\phi}$ for each of TT and EE. These modulated rational function models are very good fits to the ΛCDM spectra, but there is still a small residual. We therefore make the replacement $\hat{r}_1(\ell) \to \hat{r}_1(\ell) + \text{residual}(\ell)$, such that at $\phi = \hat{\phi}$ the model exactly reproduces the ΛCDM spectra.

With these models in hand, we are now in the position to ask whether our observed power spectra prefer the same ϕ values as ΛCDM does. For each of TE and EE, we fit linear a three-parameter model $a_1\hat{r}_1(\ell) + a_2\hat{r}_2(\ell)\cos(2\pi\ell/L+\hat{\phi}) + a_3\hat{r}_2(\ell)\sin(2\pi\ell/L+\hat{\phi})$ to our observations in the range $225 < \ell < 2000$. This model effectively encodes a phase shift $\Delta\phi = \phi_{\rm data} - \hat{\phi} = \text{Arg}(a_2 + ia_3)$ (our main interest here) as well as a wave amplitude and an overall amplitude factor.

The resulting fits can be seen in Table 5, and are consistent with the ΛCDM expectations (i.e. the phase shifts are all consistent with zero). A graphical illustration of the fit compared to the prediction and model space can be seen in Figure 14.

TABLE 5
RESULTS OF FITTING A PHASE SHIFT IN THE OBSERVED TE AND EE SPECTRA RELATIVE TO THE ΛCDM BEST-FIT MODEL.

	TE	EE	TE+EE
a_1	1.036 ± 0.066	1.008 ± 0.032	1.014 ± 0.032
a_2	1.000 ± 0.080	0.985 ± 0.088	0.986 ± 0.061
a_3	-0.108 ± 0.080	0.108 ± 0.088	0.003 ± 0.061
$\phi_{\rm data}$ (°)	23.0	−64.9	
$\Delta\phi$ (°)	-6.2 ± 4.6	6.2 ± 5.1	0.2 ± 3.6

NOTE: In the last row, a single common phase shift is fit jointly for TE and EE while still using their individual ϕ angles. The fits are in agreement with the ΛCDM expectations.

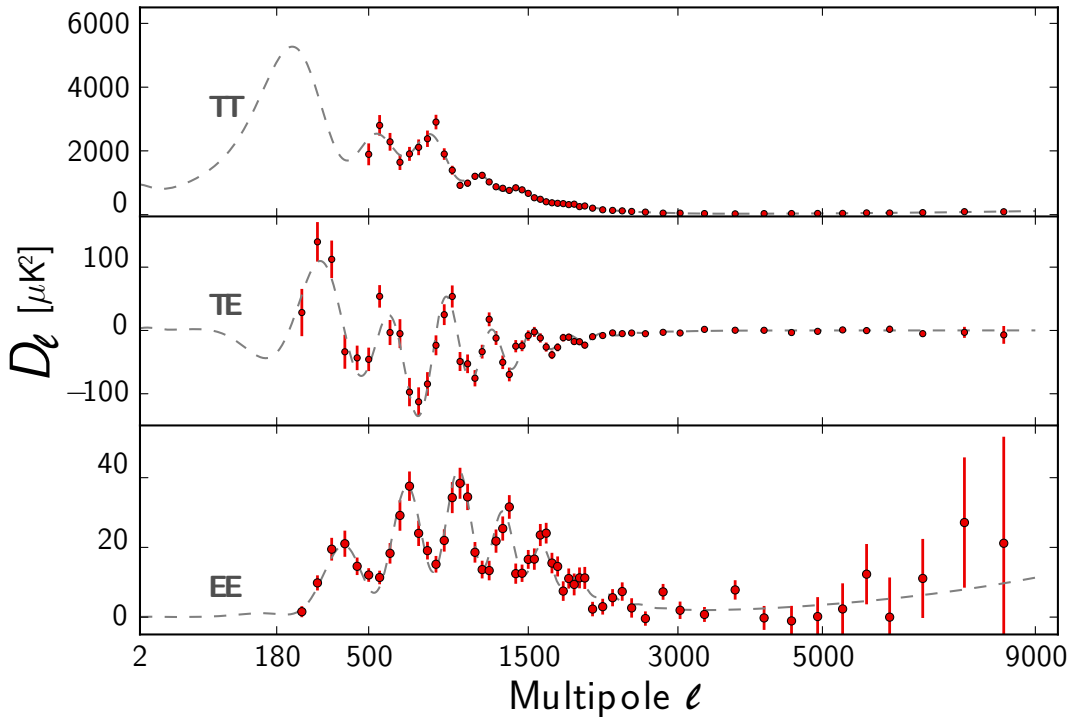

FIG. 9.— The ACTPol TT, TE, and EE power spectra, together with the best-fitting ΛCDM cosmological model and foreground components. Six acoustic peaks are seen in the E-mode polarization, out of phase with the temperature peaks and with the TE correlation pattern predicted by the standard model.

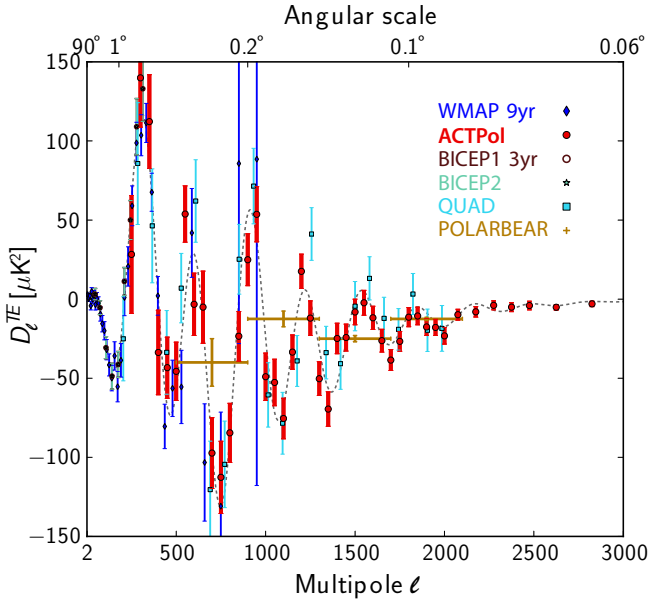

FIG. 10.— The ACTPol TE spectrum together with results from *WMAP* (Bennett et al. 2013), QUAD (QUaD Collaboration 2009), BICEP1 (BICEP1 Collaboration 2013), BICEP2 (BICEP2 Collaboration 2014a), and POLARBEAR (POLARBEAR Collaboration 2014). For ACTPol we correlate with the ACTPol temperature maps, but we could reduce error bars by also correlating with *Planck* and/or ACT temperature maps. *Planck* has shown a plot of TE and EE (Figure 11 of Planck Collaboration 2013c), but the data are not yet available.

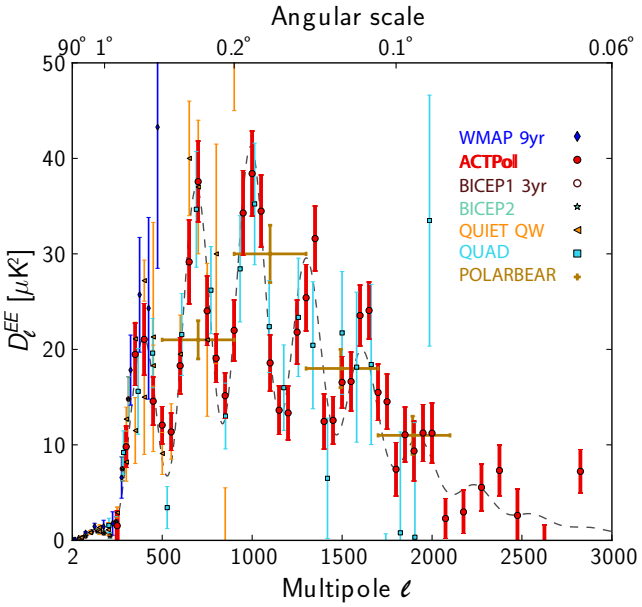

FIG. 11.— The ACTPol data together with results from other EE measurements over the past five years, as in Figure 10, and also including QUIET Q and W bands (QUIET Collaboration 2011, 2012).

4.3.3. *Polarized point sources*

We do not detect significantly polarized point sources in the ACTPol maps. Six of the highest signal-to-noise sources found in the D5 and D6 patches are shown in Figure 15; the polarization is barely detectable. For the temperature spectra, point sources above 15 mJy are masked, but no sources exceed this threshold in polarization and none are masked.

We model the Poisson tail of the temperature spectrum as

$$\mathcal{D}_\ell = (a_s + a_d)\left(\frac{\ell}{3000}\right)^2 \mu\mathrm{K}^2 \qquad (2)$$

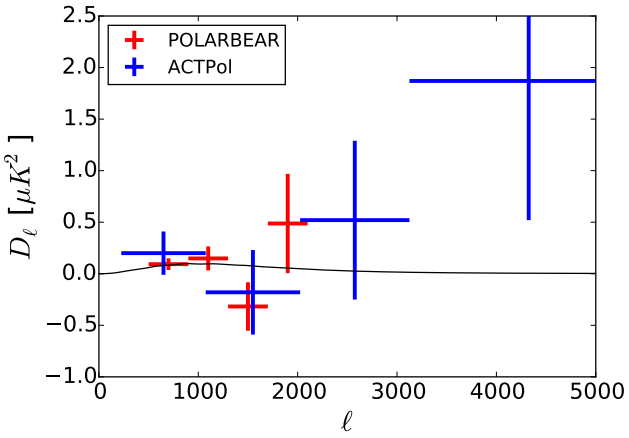

FIG. 12.— The ACTPol BB data rebinned into four bins, together with data from (POLARBEAR Collaboration 2014). The black curve shows the expected power from lensing B-modes. The ACTPol data points are consistent with zero.

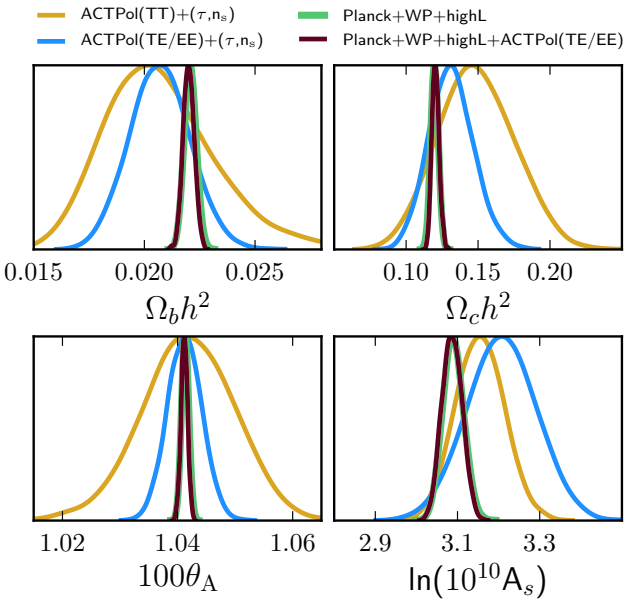

FIG. 13.— ΛCDM parameters estimated from the ACTPol TE and EE data alone(with a prior on the optical depth and spectral index from *WMAP*), and ACTPol TT alone. They are compared to the constraints from *Planck* temperature data, and combined *Planck* and ACTPol TE and EE. The temperature and polarization data give consistent results.

(Dunkley et al. 2011), where a_s is the amplitude for the residual unmasked radio/synchrotron sources and a_d is the amplitude for the pervasive dusty star forming galaxy (DSFG) or CIB component. The latter is unresolved. The two components are separated in ACT temperature measurements with two observing frequencies. In ACTPol we currently have just one frequency and so place a limit on the combined Poisson power: $a_p = a_s + a_d$. In Sievers et al. (2013) we found $a_s = 3.1 \pm 0.4$ and $a_d = 7.0 \pm 0.5$, for a total of $a_p = 10.3 \pm 0.6$ for the TT data. With the ACTPol TT data we find a consistent level of $a_p = 10.9 \pm 1.5$, for the same masking threshold.

Without masking any point sources in the EE data we find $a_p^{\rm pol} = 1.5 \pm 0.6$ at 68% confidence, or $a_p^{\rm pol} < 2.4$ at

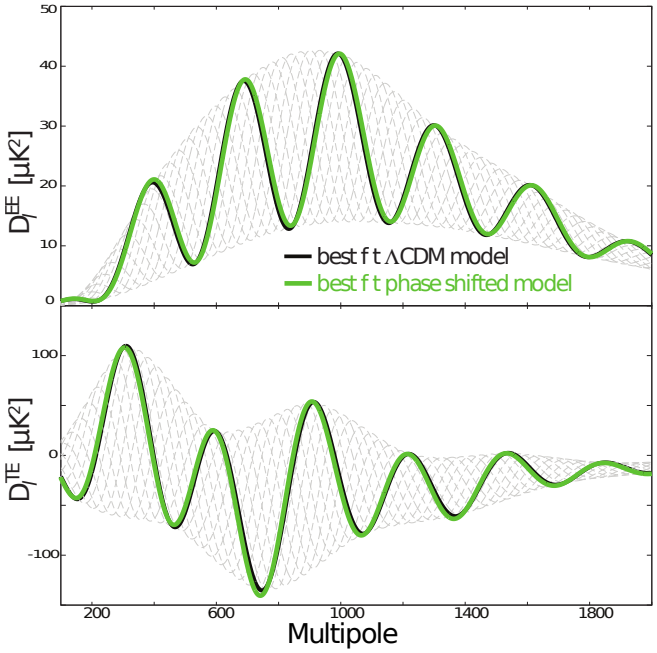

FIG. 14.— Recovered amplitudes and phases of the polarization peak/dip pattern from ACTPol data. The black curves mark the best-fit ΛCDM model power spectrum. The green curves show the best-fit amplitude/phase EE (top) and TE (bottom) models to the ACTPol data as described in the text. The thin lines in the background show the envelope of the phase-shifted model. The polarization data are in excellent agreement with the ΛCDM prediction.

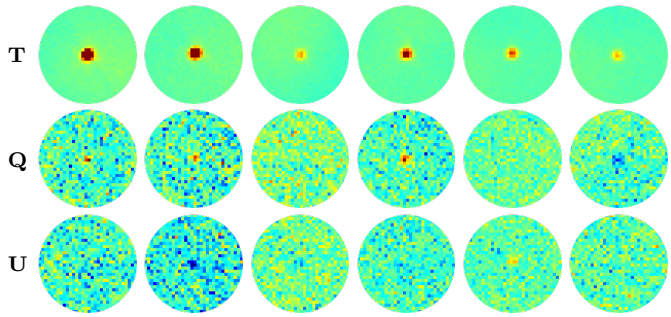

FIG. 15.— Three of the highest signal-to-noise polarized point sources from each of patch D5 (left) and D6 (right). Each disk has a radius of 8', with the value range being $\pm 2000\mu$K for T and $\pm 200\mu$K for Q and U. We do not mask polarized sources in this analysis. The sources may be associated with (from left to right) [HB89] 2332-017, [HB89] 2335-027, SDSS J001130.40+005751.7, PKS 0214-085, [HB89] 0226-038 and PKS 0205-010.

95% confidence. In flux units this corresponds to $C_\ell = 0.15^{+0.05}_{-0.07}$ Jy^2/sr, or < 0.24 Jy^2/sr (95% CL), at 146 GHz, and puts a limit on all polarized sources before masking.

5. CONCLUSIONS

The polarization capabilities of ACTPol have already enabled new probes of the cosmological model. We have shown that ACT is capable of measuring polarization to high accuracy and of measuring CMB temperature and polarization during the day. With one third of the full complement of detectors observing at night over just 90 days, we have already made some of the most competitive measurements yet of CMB polarization at $\ell > 1000$. The ACTPol EE, TE, TB, and BB data obtained to date are all in agreement with the standard model of cosmol-

ogy. We anticipate substantial improvements with more detectors and observing time.

This work was supported by the U.S. National Science Foundation through awards AST-0408698 and AST-0965625 for the ACT project, as well as awards PHY-0855887 and PHY-1214379. Funding was also provided by Princeton University, the University of Pennsylvania, and a Canada Foundation for Innovation (CFI) award to UBC. ACT operates in the Parque Astronómico Atacama in northern Chile under the auspices of the Comisión Nacional de Investigación Científica y Tecnológica de Chile (CONICYT). Computations were performed on the GPC supercomputer at the SciNet HPC Consortium. SciNet is funded by the CFI under the auspices of Compute Canada, the Government of Ontario, the Ontario Research Fund – Research Excellence; and the University of Toronto. The development of multichroic detectors and lenses was supported by NASA grants NNX13AE56G and NNX14AB58G. CM acknowledges support from NASA grant NNX12AM32H. Funding from ERC grant 259505 supports SN, JD, EC, and TL. HT is supported by grants NASA ATP NNX14AB57G, DOE DE-SC0011114, and NSF AST-1312991. BS, BK, CM, and EG are funded by NASA Space Technology Research Fellowships. R.D received funding from the CONICYT grants QUIMAL-120001 and FONDECYT-1141113. We thank our many colleagues from ABS, ALMA, APEX, and POLARBEAR who have helped us at critical junctures. Colleagues at AstroNorte and RadioSky provide logistical support and keep operations in Chile running smoothly. We thank Jesse Treu for multiple suggestions and comments. We also thank the Mishrahi Fund and the Wilkinson Fund for their generous support of the project.

REFERENCES

Ade, P. A. R., Pisano, G., Tucker, C., & Weaver, S. 2006, in Society of Photo-Optical Instrumentation Engineers (SPIE) Conference Series, Vol. 6275
Alexander, S., Ochoa, J., & Kosowsky, A. 2009, arXiv:0810.2355, Phys. Rev. D, 79, 063524
Anderson, L., et al. 2014, arXiv:1312.4877, MNRAS, 441, 24
Arendt, R. G., et al. 2011, arXiv:1103.6225, ApJ, 734, 54
Aumont, J., et al. 2010, A&A, 514, A70
Battistelli, E. S., et al. 2008, in Society of Photo-Optical Instrumentation Engineers (SPIE) Conference Series, Vol. 7020
Becker, R. H., White, R. L., & Helfand, D. J. 1995, ApJ, 450, 559
Bennett, C. L., et al. 2011, arXiv:1001.4758, ApJS, 192, 17
—. 2013, arXiv:1212.5225, ApJS, 208, 20
Betoule, M., et al. 2014, arXiv:1401.4064, A&A, 568, A22
BICEP1 Collaboration. 2013, arXiv:1310.1422
BICEP2 Collaboration. 2014a, arXiv:1403.3985
—. 2014b, arXiv:1403.4302
Bond, J. R. & Efstathiou, G. 1987, MNRAS, 226, 655
BOSS. 2014, http://www.sdss3.org/surveys/boss.php
Britton, J. W., et al. 2010, arXiv:1007.0805, in Society of Photo-Optical Instrumentation Engineers (SPIE) Conference Series, Vol. 7741
Bucher, M., Dunkley, J., Ferreira, P. G., Moodley, K., & Skordis, C. 2004, astro-ph/0401417, Physical Review Letters, 93, 081301
Calabrese, E., et al. 2013, arXiv:1302.1841, Phys. Rev. D, 87, 103012
—. 2014, arXiv:1406.4794, JCAP, 8, 10
CAPMAP Collaboration. 2008, arXiv:0802.0888, ApJ, 684, 771
CFHTLens Collaboration. 2013, arXiv:1210.8156, MNRAS, 433, 2545
Chervenak, J. A., Irwin, K. D., Grossman, E. N., Martinis, J. M., Reintsema, C. D., & Huber, M. E. 1999, Applied Physics Letters, 74, 4043
Cooray, A., Melchiorri, A., & Silk, J. 2003, astro-ph/0205214, Physics Letters B, 554, 1
Copi, C. J., Huterer, D., Schwarz, D. J., & Starkman, G. D. 2010, arXiv:1004.5602, Advances in Astronomy, 2010
Das, S., et al. 2011, arXiv:1009.0847, ApJ, 729, 62
—. 2014, arXiv:1301.1037, JCAP, 4, 14
Datta, R., et al. 2013, arXiv:1307.4715, Appl. Opt., 52, 8747
—. 2014, arXiv:1401.8029, Journal of Low Temperature Physics, Feb. 2014
de Jong, J. T. A., Verdoes Kleijn, G. A., Kuijken, K. H., & Valentijn, E. A. 2013, arXiv:1206.1254, Experimental Astronomy, 35, 25
DES. 2014, https://www.darkenergysurvey.org/index.shtml
Dicke, R. H. 1946, Review of Scientific Instruments, 17, 268
Driver, S. P., et al. 2009, arXiv:0910.5123, Astronomy and Geophysics, 50, 050000
Dunkley, J., et al. 2011, arXiv:1009.0866, ApJ, 739, 52
—. 2013, arXiv:1301.0776, JCAP, 7, 25
Dünner, R., et al. 2013, arXiv:1208.0050, ApJ, 762, 10
Durret, F., et al. 2011, arXiv:1109.0850, A&A, 535, A65
Finkbeiner, D. P., Davis, M., & Schlegel, D. J. 1999, astro-ph/9905128, ApJ, 524, 867
Fowler, J. W., et al. 2007, astro-ph/0701020, Appl. Opt., 46, 3444
Galli, S., et al. 2014, arXiv:1403.5271
Garilli, B., et al. 2014, arXiv:1310.1008, A&A, 562, A23
Górski, K. M., Hivon, E., Banday, A. J., Wandelt, B. D., Hansen, F. K., Reinecke, M., & Bartelmann, M. 2005, astro-ph/0409513, ApJ, 622, 759
Grace, E., et al. 2014, ACTPol: on-sky performance and characterization
Grace, E. A., et al. 2014, Journal of Low Temperature Physics
Güsten, R., Nyman, L. Å., Schilke, P., Menten, K., Cesarsky, C., & Booth, R. 2006, A&A, 454, L13
Hamaker, J. P. & Bregman, J. D. 1996, A&AS, 117, 161
Hanson, D., et al. 2013, arXiv:1307.5830, Physical Review Letters, 111, 141301
Hasselfield, M., et al. 2013, arXiv:1303.4714, ApJS, 209, 17
Hester, J. J. 2008, ARA&A, 46, 127
Hincks, A. D., et al. 2010, arXiv:0907.0461, ApJS, 191, 423
Hinshaw, G., et al. 2013, arXiv:1212.5226, ApJS, 208, 19
Hou, Z., et al. 2014, arXiv:1212.6267, ApJ, 782, 74
Hubmayr, J., et al. 2012, Journal of Low Temperature Physics, 167, 904
Jeong, D., Chluba, J., Dai, L., Kamionkowski, M., & Wang, X. 2014, arXiv:1309.2285, Phys. Rev. D, 89, 023003
Kamionkowski, M., Kosowsky, A., & Stebbins, A. 1997, astro-ph/9609132, Physical Review Letters, 78, 2058
Keating, B. G., Shimon, M., & Yadav, A. P. S. 2013, arXiv:1211.5734, ApJ, 762, L23
Kosowsky, A., Kahniashvili, T., Lavrelashvili, G., & Ratra, B. 2005, astro-ph/0409767, Phys. Rev. D, 71, 043006
Louis, T., Næss, S., Das, S., Dunkley, J., & Sherwin, B. 2013, arXiv:1306.6692, MNRAS, 435, 2040
Louis, T., et al. 2014, arXiv:1403.0608
Lue, A., Wang, L., & Kamionkowski, M. 1999, astro-ph/9812088, Physical Review Letters, 83, 1506
Macías-Pérez, J. F., Mayet, F., Aumont, J., & Désert, F.-X. 2010, arXiv:0802.0412, ApJ, 711, 417
MacTavish, C. J., et al. 2006, astro-ph/0507503, ApJ, 647, 799
Manzotti, A., Hu, W., & Benoit-Lévy, A. 2014, arXiv:1401.7992
Næss, S. & Louis, T. 2013, arXiv:1309.7473
Niemack, M. D., et al. 2010, arXiv:1006.5049, in Society of Photo-Optical Instrumentation Engineers (SPIE) Conference Series, Vol. 7741
Oliver, S. J., et al. 2012, arXiv:1203.2562, MNRAS, 424, 1614
Pappas, C. G., et al. 2014, Journal of Low Temperature Physics
Planck Collaboration. 2013a, arXiv:1303.5062
—. 2013b, arXiv:1312.1300
—. 2013c, arXiv:1303.5076

TABLE 6
COMBINED POWER SPECTRA, $\mathcal{D}_\ell = \ell(\ell+1)C_\ell/2\pi$ (μK^2), SHOWN IN FIGURES 6 AND 9.[a]

ℓ	ℓ range	TT		TE		EE		BB		TB		EB	
		$\mathcal{D}_\ell$	$\sigma(\mathcal{D}_\ell)$	$\mathcal{D}_\ell$	$\sigma(\mathcal{D}_\ell)$	$\mathcal{D}_\ell$	$\sigma(\mathcal{D}_\ell)$	$\mathcal{D}_\ell$	$\sigma(\mathcal{D}_\ell)$	$\mathcal{D}_\ell$	$\sigma(\mathcal{D}_\ell)$	$\mathcal{D}_\ell$	$\sigma(\mathcal{D}_\ell)$
250	225 − 275	4049.4	1476.4	28.3	37.3	1.5	1.6	0.1	1.2	25.1	25.9	0.8	0.9
300	275 − 325	3366.7	788.5	139.9	31.2	9.8	2.2	1.4	0.8	8.5	17.3	1.2	0.9
350	325 − 375	2377.3	510.0	112.2	29.7	19.5	3.3	0.3	0.7	-5.7	12.4	0.6	0.9
400	375 − 425	1366.2	376.3	-33.7	26.8	21.0	3.8	1.0	0.7	9.3	11.4	0.5	1.1
450	425 − 475	1683.2	310.0	-43.3	19.4	14.6	2.5	1.1	0.7	10.9	9.2	0.2	0.9
500	475 − 525	1892.9	342.9	-45.6	18.5	12.1	2.0	-0.2	0.7	23.4	10.4	0.1	0.8
550	525 − 575	2801.0	323.5	53.8	17.8	11.4	2.0	0.3	0.7	-14.1	9.8	-0.7	0.8
600	575 − 625	2284.9	278.6	-3.3	19.8	18.3	3.0	-0.3	0.8	-11.5	9.1	-0.1	1.0
650	625 − 675	1644.6	242.7	-5.1	22.8	29.2	4.4	-0.7	0.8	4.9	9.3	-0.1	1.2
700	675 − 725	1907.0	218.9	-97.3	22.4	37.6	4.2	-0.2	0.8	-4.8	8.6	1.2	1.2
750	725 − 775	2112.9	246.5	-112.6	22.8	24.0	3.6	0.6	0.8	-2.4	8.8	-0.3	1.1
800	775 − 825	2381.3	257.2	-84.5	18.7	19.1	2.5	-1.0	1.0	-4.9	10.0	0.7	1.0
850	825 − 875	2904.4	228.6	-23.5	15.7	15.2	2.4	0.3	1.0	4.2	9.1	1.1	1.0
900	875 − 925	1901.5	181.3	24.9	16.4	22.0	3.2	1.1	1.0	13.0	8.3	0.1	1.2
950	925 − 975	1393.4	140.3	53.6	17.4	34.3	4.5	-1.0	1.2	-9.0	8.2	1.8	1.5
1000	975 − 1025	920.8	109.2	-49.0	15.0	38.4	4.5	-1.4	1.1	8.8	7.1	-0.1	1.5
1050	1025 − 1075	987.4	107.8	-52.7	14.7	34.5	3.8	-0.4	1.4	-4.3	7.5	1.5	1.4
1100	1075 − 1125	1203.5	105.2	-75.5	12.9	18.6	3.0	-0.0	1.3	-17.4	7.6	0.6	1.3
1150	1125 − 1175	1234.2	107.1	-33.5	10.9	13.6	2.5	-0.9	1.4	9.4	7.6	1.3	1.3
1200	1175 − 1225	1026.2	90.6	17.6	10.9	13.3	2.8	0.6	1.5	-2.8	7.2	0.7	1.5
1250	1225 − 1275	875.3	74.9	-12.0	10.9	21.8	3.3	-1.4	1.5	4.8	6.9	-1.8	1.5
1300	1275 − 1325	828.4	65.6	-50.3	10.7	25.4	3.5	-0.7	1.5	8.6	6.3	-0.8	1.5
1350	1325 − 1375	761.1	67.4	-69.5	10.9	31.6	3.4	2.0	1.7	-7.0	6.8	1.5	1.7
1400	1375 − 1425	843.5	66.0	-24.9	9.7	12.5	2.9	1.2	1.7	-6.0	6.5	-1.2	1.5
1450	1425 − 1475	778.9	60.2	-24.3	8.5	12.6	2.5	-2.3	1.7	-5.9	6.6	0.7	1.4
1500	1475 − 1525	668.3	54.3	-8.1	8.1	16.5	2.7	-1.2	1.7	-13.7	6.2	-0.5	1.5
1550	1525 − 1575	530.9	42.9	-2.3	7.9	16.6	3.1	-1.5	2.0	-3.2	5.8	-1.0	1.7
1600	1575 − 1625	482.7	37.1	-11.8	7.3	23.5	3.2	-0.4	1.9	-5.5	5.3	-1.8	1.7
1650	1625 − 1675	404.7	33.2	-26.2	7.2	24.1	3.0	-0.6	2.1	-5.5	5.2	-0.5	1.7
1700	1675 − 1725	372.8	31.6	-38.5	6.6	15.5	2.9	-0.7	2.0	-2.8	5.1	-1.5	1.7
1750	1725 − 1775	356.3	31.0	-26.7	6.2	14.5	2.9	2.7	2.3	9.3	5.4	-0.5	1.7
1800	1775 − 1825	346.6	28.8	-11.4	6.1	7.5	2.8	-1.3	2.2	0.7	5.1	-1.3	1.7
1850	1825 − 1875	315.5	24.4	-10.6	5.6	11.1	2.9	0.4	2.4	-0.9	4.7	0.2	1.8
1900	1875 − 1925	330.0	22.2	-17.6	5.4	9.4	3.1	-0.7	2.5	3.8	4.7	0.9	1.9
1950	1925 − 1975	252.6	20.4	-17.9	5.1	11.2	3.0	4.8	2.5	-0.4	4.4	-0.6	1.8
2000	1975 − 2025	272.6	19.1	-23.2	5.2	11.2	3.2	0.2	2.7	-2.3	4.6	-0.9	2.0
2075	2025 − 2125	204.5	12.5	-9.8	3.5	2.3	2.1	0.8	1.9	-0.7	3.1	0.3	1.4
2175	2125 − 2225	153.2	10.3	-8.0	3.3	3.0	2.3	-2.5	2.1	-1.5	2.9	2.1	1.5
2275	2225 − 2325	133.9	8.3	-3.9	2.9	5.6	2.5	-1.5	2.2	1.1	2.8	0.3	1.6
2375	2325 − 2425	120.1	7.4	-5.1	2.9	7.3	2.6	0.6	2.3	-2.6	2.7	1.0	1.7
2475	2425 − 2525	101.4	6.7	-4.0	2.8	2.6	2.8	3.1	2.5	2.7	2.6	1.3	1.8
2625	2525 − 2725	81.1	4.1	-5.1	1.8	-0.4	2.1	4.3	1.9	-0.4	1.7	1.3	1.3
2825	2725 − 2925	48.6	3.5	-3.0	1.8	7.2	2.3	-1.3	2.2	0.9	1.7	-0.0	1.5
3025	2925 − 3125	49.2	3.1	-4.0	1.8	1.9	2.5	0.1	2.5	-0.3	1.7	0.1	1.7
3325	3125 − 3525	34.7	2.2	1.7	1.3	0.7	2.1	0.5	2.1	-0.5	1.3	0.3	1.5
3725	3525 − 3925	25.9	2.3	0.3	1.6	7.8	2.8	3.2	2.7	-0.1	1.5	0.6	1.8
4125	3925 − 4325	33.7	2.6	0.2	1.8	-0.3	3.4	2.3	3.4	0.6	1.8	0.3	2.3
4525	4325 − 4725	35.7	3.2	-3.3	2.3	-1.1	4.3	1.1	4.5	3.0	2.3	1.0	2.9
4925	4725 − 5125	38.2	3.9	-1.4	2.9	0.1	5.6	-0.2	5.6	0.7	2.8	2.1	3.9
5325	5125 − 5525	40.9	4.5	0.8	3.5	2.3	7.4	11.7	7.1	-6.7	3.5	-7.0	4.9
5725	5525 − 5925	55.8	5.7	-0.2	4.3	12.3	8.7	24.4	8.9	1.6	4.2	-8.7	6.0
6125	5925 − 6325	52.7	6.9	1.8	5.6	-0.0	11.4	2.6	11.2	-0.5	5.3	1.5	7.7
6725	6325 − 7125	65.0	7.2	-5.1	5.3	11.1	11.3	12.6	11.3	4.0	5.4	11.9	7.7
7525	7125 − 7925	94.3	12.0	-3.0	8.7	27.1	18.7	43.0	17.9	-2.9	8.6	25.5	12.7
8325	7925 − 8725	91.6	18.7	-7.0	14.0	21.2	30.6	18.6	30.3	14.4	14.0	14.1	20.8

[a]The overall temperature map calibration error is 2%.

—. 2013d, arXiv:1303.5083
—. 2014, arXiv:1405.0871
QUaD Collaboration. 2009, arXiv:0906.1003, ApJ, 705, 978
QUIET Collaboration. 2011, arXiv:1012.3191, ApJ, 741, 111
—. 2012, arXiv:1207.5034, ApJ, 760, 145
Readhead, A. C. S., et al. 2004, astro-ph/0409569, Science, 306, 836
Rocha, G., Trotta, R., Martins, C. J. A. P., Melchiorri, A., Avelino, P. P., Bean, R., & Viana, P. T. P. 2004, astro-ph/0309211, MNRAS, 352, 20
SDSS. 2014, http://www.sdss.org
Shimon, M., Keating, B., Ponthieu, N., & Hivon, E. 2008, arXiv:0709.1513, Phys. Rev. D, 77, 083003
Sievers, J. L., et al. 2007, astro-ph/0509203, ApJ, 660, 976
—. 2013, arXiv:1301.0824, JCAP, 10, 60
Spergel, D. N., et al. 2003, astro-ph/0302209, ApJS, 148, 175
Story, K. T., et al. 2013, arXiv:1210.7231, ApJ, 779, 86
Subaru. 2014, http://www.naoj.org/Projects/HSC/
Suzuki, N., et al. 2012, arXiv:1105.3470, ApJ, 746, 85
Swetz, D. S., et al. 2011, arXiv:1007.0290, ApJS, 194, 41
POLARBEAR Collaboration. 2013, arXiv:1312.6645
—. 2014, arXiv:1403.2369
Tucker, C. E. & Ade, P. A. R. 2006, in Society of Photo-Optical Instrumentation Engineers (SPIE) Conference Series, Vol. 6275
Véron-Cetty, M.-P. & Véron, P. 2006, A&A, 455, 773
Viero, M. P., et al. 2014, arXiv:1308.4399, ApJS, 210, 22
Weiland, J. L., et al. 2011, arXiv:1001.4731, ApJS, 192, 19
White, R. L., Becker, R. H., Helfand, D. J., & Gregg, M. D. 1997, VizieR Online Data Catalog, 8048, 0
XMM-XXL. 2014, http://sci.esa.int/xmm-newton/48357-xxl-the-ultimate-xmm-extragalactic-survey/

Zaldarriaga, M. & Seljak, U. 1997, astro-ph/9609170, Phys. Rev. D, 55, 1830

—. 1998, astro-ph/9803150, Phys. Rev. D, 58, 023003